

## Improved parameterization of seagrass blade dynamics and wave attenuation based on numerical and laboratory experiments

Robert B. Zeller,\* Joel S. Weitzman, Morgan E. Abbett, Francisco J. Zarama, Oliver B. Fringer, and Jeffrey R. Koseff

Environmental Fluid Mechanics Laboratory, Department of Civil and Environmental Engineering, Stanford University, Stanford, California

### *Abstract*

Seagrass blade dynamics were explored through numerical and laboratory experiments in order to improve parameterization of wave attenuation by submerged aquatic vegetation in the presence of a background current. In the numerical model, a single blade was modeled as a series of rigid plates attached by torsion springs. For the laboratory model, strips of low-density polyethylene were placed in a recirculating wave flume. A new form of the Keulegan–Carpenter number based on the horizontal excursion of the blade tip was found to be an excellent predictor of drag coefficient. An algebraic model for predicting wave attenuation was developed based on the following observations. During the portion of the wave period when the fluid velocities are highest, the blade motion is almost completely arrested and the vast majority of the turbulence production occurs during this time. Turbulence production when the blade is pronated is accurately predicted by the maximum fluid velocity over the wave period. The relative contribution to the total turbulence production over the wave period is determined by the relative strength of the waves and the current. Therefore, using a simple algebraic fit, the total depth-integrated, time-averaged turbulence production can be accurately predicted by two flow parameters: the maximum fluid velocity over the wave period, and a non-dimensional number that compares the wave and current velocities. By fitting the algebraic model to data from a particular site, it can be used to efficiently estimate wave attenuation and drag coefficient in seagrass exposed to waves with a background current.

Seagrasses have long been recognized for their ability to attenuate wave energy in the coastal environment (Ward et al. 1984; Fonseca and Fisher 1986; Fonseca and Cahalan 1992). As coastal ecosystems change in response to climate change and direct anthropogenic stresses, proper accounting of wave attenuation by vegetation will be crucial to ecosystem management (Duarte 2002; Chen et al. 2007). This accounting is accomplished by incorporating simplified vegetation models into larger scale coastal models. An effective vegetation model must factor in essential vegetation parameters (e.g., geometry, rigidity, morphology) to accurately translate fluid velocities from a large-scale model into estimated wave attenuation. Because wave attenuation is a large-scale process that depends on small-scale interactions, it is studied on multiple scales using different methodologies. In order to understand how the results in the present work will help to improve large-scale modeling, vegetative wave attenuation research can be categorized into three main areas, each at a different scale: (1) the development of mechanistic understanding of wave attenuation at the blade or canopy scale in order to create well-parameterized models ( $10^{-1}$ – $10^0$  m); (2) the refinement of vegetative wave attenuation models at the meadow scale by examining them over the parameter space of realistic field conditions ( $10^1$ – $10^2$  m); and (3) the incorporation of vegetative wave attenuation models into ecosystem- or coastal-scale ocean models and validation with field measurements ( $10^2$ – $10^3$  m). The present study focuses on

improving mechanistic understanding and parameterization of wave attenuation in flexible vegetation (research area ‘1’).

It is important to understand how energy is removed from the waves and where this energy goes. In the case of vegetative wave attenuation, the removal of wave energy is accomplished by the work done on the fluid by the vegetation. Mathematically, the rate of this work is equal to the relative velocity between the fluid and the vegetation multiplied by the component of the force that the vegetation applies to the fluid acting in the direction of the relative velocity, integrated over all vegetation surfaces (see Eq. 7). This essentially quantifies how much the vegetation resists the motion of the fluid, thereby removing energy from the mean flow. This removal can be thought of as wave energy dissipation. However, if the characteristic vegetation scale is larger than the scale at which energy is dissipated by turbulence (i.e., Reynolds number based on blade width is large), the energy extracted from the mean flow is not simply dissipated into heat, but is transferred into turbulent kinetic energy. The production of turbulence has important implications other than dissipation of wave energy, such as mixing of nutrients. In this paper, in order to emphasize the fact that energy is being diverted into an important physical phenomenon, the transfer of energy from waves to turbulence is referred to as turbulence production. The amount of turbulent kinetic energy produced is equivalent to the amount of wave energy that is dissipated by the vegetation. Because direct computation of this energy transfer requires detailed information about

\* Corresponding author: rzeller@stanford.edu

the fluid velocity and the forces imposed by the vegetation, it can only be done in small-scale numerical models.

Previous numerical efforts to develop mechanistic understanding and improve parameterization of drag in seagrass have simplified key aspects of the real system. Specifically, numerical models have not allowed for both unsteady flow and arbitrary flexural rigidity. Flexural rigidity refers to the vegetation's resistance to bending, which is important for understanding the dynamics of seagrass motion. Although the elasticity of flexible aquatic vegetation allows for both bending and stretching of the plant material, the stretching of seagrass blades can be neglected because the tensile stresses are extremely small. For kelp, stretching can be important, so it has been included in unsteady models of kelp exposed to waves (Utter and Denny 1996; Denny et al. 1998). In order to better understand the region of parameter space that the present numerical model addresses, seagrass blade dynamics can be framed in terms of non-dimensional parameters, which are created by normalizing each of the forces acting on the vegetation by the drag force. In this context, the rigidity of the blade is quantified with  $\lambda_R$ , which compares the rigidity of the blade to the drag force (Ghisalberti and Nepf 2002):

$$\lambda_R = \frac{Eb^3}{\rho_w L^3 U_{\max}^2} \quad (1)$$

where  $E$  is Young's modulus of elasticity,  $b$  is the thickness of the blade,  $\rho_w$  is the density of water,  $L$  is the length of the blade, and  $U_{\max}$  is the maximum phase-averaged free-stream velocity over the wave period. In the current paper,  $\lambda_R$  is used to predict blade pronation and  $U_{\max}$  is chosen to scale the drag because the blade is pronated when the wave velocity is highest. The inclusion of rigidity makes the equations governing blade motion more strongly coupled and therefore more difficult to solve. The blade rigidity acts on a time scale that is much shorter than the time scale of the problem. Small fluctuations near the stem result in large forces at the blade tip, making the system numerically unstable. To avoid these issues, most numerical studies of blade bending have focused on cases when  $\lambda_R$  is arbitrarily large or small. Ignoring rigidity ( $\lambda_R \ll 1$ ), Abdelrhman (2007) modeled a seagrass blade in a steady flow as a series of rectangular plates and found the steady-state position of the blade based on a force balance. Assuming small deflections ( $\lambda_R \gg 1$ ), Mullarney and Henderson (2010) and Riffe et al. (2011) studied wave attenuation by linearizing the Euler–Bernoulli equation and solving it analytically. Luhar and Nepf (2011) employed a shooting method to study large deflections ( $\lambda_R \sim 1$ ), but their method is limited to steady flows. Many seagrasses in their natural environment are exposed to waves and experience large deflections that are primarily governed by a balance between rigidity and drag, such that  $\lambda_R \sim 1$ . This paper describes the development of a numerical model that addresses this important region of parameter space.

The primary way that vegetative wave attenuation is incorporated into large-scale models (research area '3') is through an effective drag coefficient, ( $C_D$ ; Dalrymple et al.

1984; Kobayashi et al. 1993; Mendez and Losada 2004). To do this, the elements are assumed to be rigid with their full frontal area exposed to the flow. The value of  $C_D$  is chosen to account for the reduced velocities and reduced frontal area associated with element flexibility.  $C_D$  depends on both flow and vegetation parameters and is typically estimated from empirical relationships.  $C_D$  is used to compute drag in a momentum equation or dissipation in a wave energy equation, depending on the model. An example of using  $C_D$  to account for dissipation of wave energy is a vegetation module that was implemented in the Simulating WAVes Nearshore model (SWAN-VEG; Oude 2010). Because  $C_D$  depends on the complex dynamics of flexible vegetation in waves, improving estimates of  $C_D$  is an area of ongoing research.

A popular way of predicting  $C_D$  is by relating it to a Keulegan–Carpenter number ( $KC$ ), which compares the wake development scale to the size of the obstacle (Mendez and Losada 2004; Sánchez-González et al. 2011; Infantes et al. 2012). Much of the research in realistic conditions with live vegetation (research area '2') has been structured around this model. The practice of relating drag coefficient to  $KC$  originates from the coastal engineering literature, where it is used to predict drag on piles exposed to waves (Dean and Dalrymple 1991). Although the estimates are accurate for an individual rigid cylinder, such as a pile, they lose accuracy in flexible aquatic vegetation primarily for three reasons. (1) The motion of the vegetation alters the relative velocity between the fluid and the vegetation, which can have a significant effect on  $C_D$  (Bradley and Houser 2009). (2) The frontal area of the seagrass is reduced when the elements become pronated. (3) The grouping of elements into canopies results in reduced wave velocities inside the canopy (Lowe et al. 2005; Luhar et al. 2010), a complexity that will be explored in future work.

$KC$  can be viewed as a comparison of a length scale of wake development— $L_{\text{development}}$ —with a length scale of the geometry— $L_{\text{geometry}}$ . Assuming that the wake development scales with the velocity of the fluid, the freestream orbital excursion of the waves,  $A_{\text{rms}}^{\infty}$ , gives a scale for the wake development over one wave period.  $A_{\text{rms}}^{\infty} = U_{\text{rms}}^{\infty} T(2\pi)^{-1}$ , where  $U_{\text{rms}}^{\infty}$  is the root-mean-square of the freestream streamwise wave component of the velocity and  $T$  is the wave period.

$$KC = \frac{L_{\text{development}}}{L_{\text{geometry}}} = \frac{A_{\text{rms}}^{\infty}}{L_{\text{geometry}}} \quad (2)$$

The choice of  $L_{\text{geometry}}$  is critical and depends on the application. The width of the canopy elements has been used for both rigid and flexible canopies (Bradley and Houser 2009), a choice that follows from canonical consideration of wave forces on vertical piles. Canopy spacing has also been suggested as the relevant length scale for rigid canopies (Lowe et al. 2005). Although these length scales may be appropriate for certain applications, conditions in a flexible canopy are dependent on blade bending, and the length scale in  $KC$  should reflect this dependence.

In the present study, the blade-bending excursion ( $L_{\text{BBE}}$ ), defined as the horizontal excursion of the blade tip, was

explored as a more appropriate length scale for the vegetation. The resulting form of  $KC$  is denoted  $KC_{\text{BBE}} \equiv \frac{A_{\text{rms}}^{\infty}}{L_{\text{BBE}}}$ .  $KC_{\text{BBE}}$  was found to be a much better predictor of  $C_D$  because it accounts for blade bending. This is not necessarily a practical approach because it requires a priori knowledge of the blade motion. However, the strength of the relationship between  $C_D$  and  $KC_{\text{BBE}}$  demonstrates the fundamental problem with previous versions of  $KC$ : they characterize the magnitude of the flow without capturing the effects of bending.

Another predictive method found in the literature is to relate  $C_D$  to  $Re$  (Kobayashi et al. 1993; Mendez and Losada 2004; Bradley and Houser 2009), where the length scale in  $Re$  is the blade width. This approach is inadequate for the same reason as previous versions of  $KC$ ; it does not properly account for blade bending.  $Re$  is a measure of the scale separation between the wake turbulence and the dissipative scales, which has little to do with the physical mechanisms that cause  $C_D$  to vary in flexible vegetation. In reality,  $Re$  and  $KC$  based on blade width are only useful as measures of the flow strength. When the flow gets stronger, the drag coefficient decreases either because the vegetation moves with the flow or because the vegetation becomes streamlined. The fitting parameters are different for each field site because the vegetation reacts differently to the flow. Although wave attenuation could be predicted by a parameter that accounts for blade motion, such as  $KC_{\text{BBE}}$ , this would require extensive measurements of vegetation properties and modeling of the blade dynamics. Instead, it is more practical to develop a predictive method with adjustable parameters that account for vegetation morphology. Although this is essentially how the aforementioned  $Re$  and  $KC$  parameterizations have been used, an improved method that accounts for the issues raised above would have a clear connection to physical mechanisms and would be applicable to more complex flows. Such a method is proposed in this text.

In the present study, a simple model of seagrass blade dynamics was developed in order to explore the physical parameters that most strongly influence wave attenuation. The model allows easy manipulation of key parameters and a complete spatio-temporal record of the force interactions between the blade and the fluid. The model is novel because it accounts for blade rigidity in the presence of unsteady fluid motion without assuming small deflections, as in Mullarney and Henderson (2010). Laboratory experiments with model seagrass blades were used to validate the numerical model and to develop qualitative understanding of the blade motion. Observations from the numerical and laboratory results led to the development of an algebraic model for predicting vegetative wave attenuation in oscillatory flow with a background current.

The objectives of this paper are to (1) describe and validate the numerical and laboratory models, (2) present results and observations from these two models, (3) describe the development of the proposed algebraic model for wave attenuation, and (4) explain the significance of the results and how they will influence future work. The Methods section describes the development of the numer-

ical model and the details of the laboratory model. The Results section presents validation of the laboratory and numerical models, a demonstration of the improved  $KC$  parameterization, the development of the algebraic model, and a comparison between the algebraic model and previous parameterizations. The Discussion addresses practical application of the model, scaling from individual blades to a canopy, and the physical mechanisms by which seagrass acts as a low-pass filter.

## Methods

*Numerical model*—A single blade of seagrass was conceptually modeled as a series of rigid rectangular plates attached with torsion springs at the joints (Fig. 1a). The torsion springs were incorporated to account for the rigidity of the blade. A system of ordinary differential equations (ODEs) was derived from horizontal and vertical force balances and a moment balance for each blade segment. The balances included the forces associated with buoyancy, lift, form drag, skin friction, and hydrodynamic inertial effects, as well as the moments from the torsion springs. Linear damping of relative angular velocity between segments, conceptually represented with rotary dashpots, was included in order to damp out spurious oscillations. All of the hydrodynamic forces are based on the translation of rigid plates with the velocities defined by the velocities at the centers of the plates. The lift, drag, and skin friction are based on Abdelrhman (2007) and the hydrodynamic inertial forces are based on Utter and Denny (1996). A free body diagram is provided in Fig. 1b. The force parameterizations are summarized in Table 1 and additional details can be found in the Web Appendix ([www.aslo.org/lo/toc/vol\\_59/issue\\_1/0251a.pdf](http://www.aslo.org/lo/toc/vol_59/issue_1/0251a.pdf)).

Because the most novel addition to the model is the rigidity, the torsion spring discretization is described here. According to the Euler–Bernoulli equation (Ghisalberti and Nepf 2002), the internal moment in a short segment of a bent blade ( $M_I$ ) is

$$M_I = E_i I_i \frac{\partial^2 \zeta}{\partial s^2} \quad (3)$$

$E_i$  is the Young's Modulus of the  $i$ th blade segment,  $I_i$  is the area moment of inertia of the  $i$ th blade segment's cross-section,  $\zeta$  is the displacement of the blade, and  $s$  is the dimension along the blade. The blade is discretized into a series of linear segments, such that  $\partial \zeta / \partial s = \sin \theta_{s,i}$ , where  $\theta_{s,i}$  is the angle of the displaced  $i$ th segment relative to  $s$ . Assuming small displacements from the local blade angle,  $\sin \theta_{s,i} \approx \theta_{s,i}$ . This assumption allows for large blade deflections as long as the blade is discretized into enough segments. By discretizing the second derivative with respect to  $s$ , the internal moment is found to be proportional to the difference between the angles of adjacent segments:

$$M_I = E_i I_i \frac{\theta_{i-1} - \theta_i}{L/n} \quad (4)$$

where  $\theta_i$  is the  $i$ th segment's angle from vertical and  $n$  is the number of segments used in the discretization. This

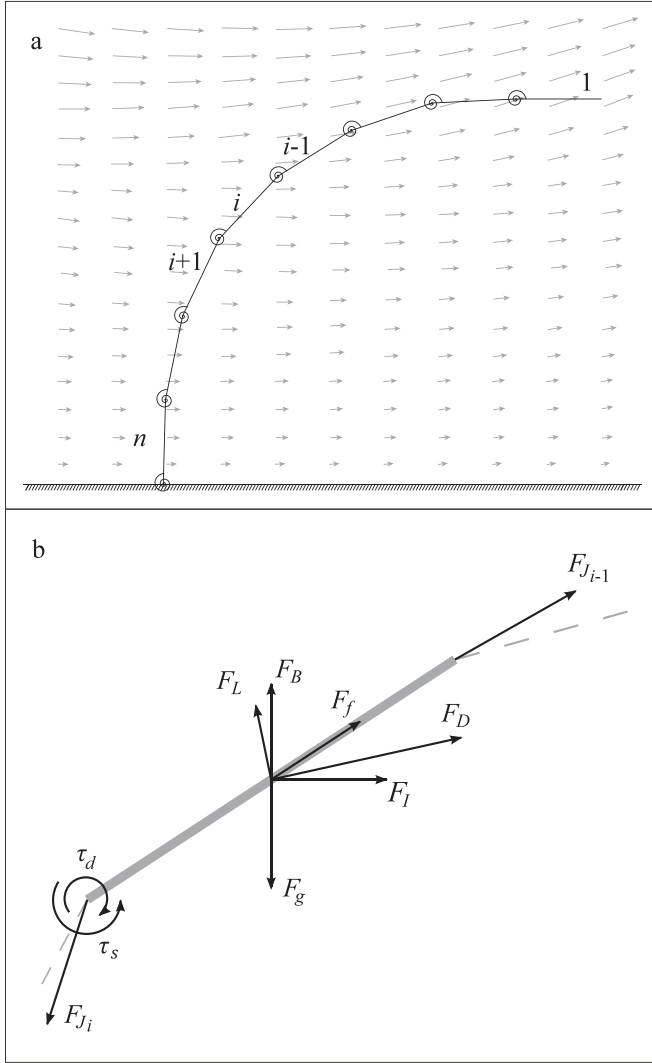


Fig. 1. (a) Schematic of the numerical model blade showing torsion springs. (b) Free body diagram for a single numerical blade segment. Forces and moments include the following: forces from adjacent blade segments,  $F_{J_i}$  and  $F_{J_{i-1}}$ ; skin friction,  $F_f$ ; drag  $F_D$ ; lift  $F_L$ ; buoyancy,  $F_B$ ; hydrodynamic inertial forces,  $F_I$ ; gravity,  $F_g$ ; torque by torsion spring,  $\tau_s$ ; and damping by rotary dashpots,  $\tau_d$ .

proportionality gives the spring constant,  $\beta_i = nE_i I_i L^{-1}$ , such that

$$M_I = \beta_i(\theta_{i-1} - \theta_i) \quad (5)$$

The relationship can be adjusted to account for blades that curve naturally when no force is applied:

$$M_I = \beta_i(\theta_{i0} - (\theta_{i-1} - \theta_i)) \quad (6)$$

where  $\theta_{i0}$  is the un-displaced angle of the  $i$ th blade segment.

The model takes phase-averaged velocity profiles as inputs, and then spatially and temporally interpolates the values for each blade segment in order to compute the forces that act on that segment. All model runs presented in this paper were forced with velocities based on laboratory measurements. The initial position of the blade was slightly

displaced from vertical, but the initial condition has little effect on the steady-state blade motion. Blades were composed of 20 segments in all model runs. The system of ODEs was solved numerically using a stiff ODE solver in MATLAB®, ODE15S. There is a region of parameter space where the solution does not converge because the problem becomes ill-conditioned. This typically occurs at extremely low  $\lambda_R$  ( $\ll 10^{-2}$ ). At these values, the blade can curl over, such that the reverse motion of the wave causes the blade to fold on itself. Laboratory observations suggest that this folding is overcome by twisting of the blade, a phenomenon that cannot be captured by a two-dimensional model. The direct output of the model is the blade segment angles and angular velocities as a function of time. Representative results for blade-tip location as a function of time are given in Fig. 2. The rapid convergence to steady state is demonstrated by the similarity between each wave period. For more details of the model formulation, see the Web Appendix.

From the model results, the position of the blade, the relative velocities between the fluid and the blade, and the forces acting on the blade can be computed for all times. The volume-integral of the turbulence production caused by the vegetation,  $P$ , is defined mathematically as

$$P = \iiint_V -\langle u'_i u'_j \rangle \frac{\partial \langle u_i \rangle}{\partial x_j} dV + \iint_S \langle p' v'_i n'_i \rangle dS \quad (7)$$

where angle brackets denote phase-averaging, primes denote fluctuations about the phase-average,  $u_i$  denotes the  $i$ th component of the fluid velocity,  $V$  denotes the control volume,  $S$  denotes the plant surfaces,  $p$  denotes pressure,  $v_i$  denotes the  $i$ th component of the velocity of the plant surface, and  $n_i$  denotes the  $i$ th component of the unit vector normal to the plant surface (Finnigan 2000). Production of turbulence due to viscous forces at the plant surface has been ignored based on high  $Re$ . Computing  $P$  from the mathematical definition in Eq. 7 could only be accomplished by using a direct numerical simulation to fully resolve the turbulence. Instead,  $P$  can be estimated by parameterizing the forces between the vegetation and the fluid. In this study, it was estimated as

$$P = \int_0^L (\vec{F}_D + \vec{F}_f) \cdot \vec{u}_{rel} ds \quad (8)$$

where  $\vec{F}_D$  and  $\vec{F}_f$  are the form drag and skin friction, respectively,  $\vec{u}_{rel}$  is the relative velocity between the blade and the fluid, and  $s$  is the dimension along the blade. The time-averaged production over the wave phase is  $\hat{P}_T = (1/T) \int_0^T P dt$ . Hydrodynamic inertial forces,  $\vec{F}_I$ , are neglected in the wave attenuation estimate in Eq. 8. In the most extreme wave accelerations, the instantaneous magnitude of  $\vec{F}_I$  was found to be at least one order of magnitude smaller than the magnitude of  $\vec{F}_D$ . Even in the runs with the largest wave accelerations and smallest current velocities, the time-integrated magnitude of  $\vec{F}_I$  was two orders of magnitude smaller than the time-integrated drag. This disparity is magnified when computing  $\hat{P}_T$  because  $\vec{F}_D$  is in phase with  $\vec{u}_{rel}$  and  $\vec{F}_I$  is not.

Table 1. Force and moment definitions for the numerical model.  $k$  is the damping coefficient of the rotary dashpots;  $\rho_w$  is the density of water,  $w_i$  and  $b_i$  are the width and thickness of the  $i$ th blade segment;  $l$  is the length of a blade segment;  $\vec{e}_z$  is a vertical unit vector;  $\rho_{g_i}$  is the density of the  $i$ th blade segment;  $\vec{u}_i$  and  $\vec{u}_i$  are the fluid velocity and acceleration at the midpoint of the  $i$ th blade segment;  $\vec{x}_i$ ,  $\dot{\vec{x}}_i$ , and  $\ddot{\vec{x}}_i$  are the position, velocity, and acceleration of the midpoint of the  $i$ th blade segment;  $\theta_{a_i}$  is the angle of attack, defined as the angle between  $\vec{u}_i$  and  $\dot{\vec{x}}_i$ ;  $c_D$ ,  $c_L$ ,  $c_f$ , and  $c_{a_i}$  are the drag, lift, friction, and added mass coefficients of the  $i$ th blade segment.

Force or moment	Definition
Torsion springs	$\tau_{s_i} = \beta_i(\theta_{0_i} - (\theta_i - \theta_{i+1}))$
Rotary dashpots	$\tau_{d_i} = -k(\dot{\theta}_i - \dot{\theta}_{i+1})$
Buoyancy	$\vec{F}_{B_i} = \rho_w g l w_i b_i \vec{e}_z$
Gravity	$\vec{F}_{g_i} = \rho_{g_i} g l w_i b_i \vec{e}_z$
Drag	$\vec{F}_{D_i} = \frac{1}{2} c_D \rho_w (\vec{u}_i - \dot{\vec{x}}_i) \ \vec{u}_i - \dot{\vec{x}}_i\  l w_i \sin(\theta_{a_i} - \theta_i)$ where $c_D = \begin{cases} \frac{1.2}{\pi/2} (\theta_{a_i} - \theta_i) & \text{if }  \theta_{a_i} - \theta_i  < \frac{\pi}{2} \\ \frac{1.2}{\pi/2} (\pi - (\theta_{a_i} - \theta_i)) & \text{if } (\theta_{a_i} - \theta_i) > \frac{\pi}{2} \\ \frac{1.2}{\pi/2} ((\theta_{a_i} - \theta_i) - \pi) & \text{if }  \theta_{a_i} - \theta_i  < -\frac{\pi}{2} \end{cases}$ and $\theta_{a_i} = \frac{\pi}{2} + \tan^{-1} \left( \frac{(\vec{u}_i - \dot{\vec{x}}_i) \cdot \vec{e}_x}{(\vec{u}_i - \dot{\vec{x}}_i) \cdot \vec{e}_z} \right)$
Lift	$\vec{F}_{L_i} = \frac{1}{2} c_L \rho_w (\vec{u}_i - \dot{\vec{x}}_i) \ \vec{u}_i - \dot{\vec{x}}_i\  l w_i \cos(\theta_{a_i} - \theta_i)$ where $c_L = \begin{cases} \frac{0.8}{15} (\theta_{a_i} - \theta_i) & \text{if }  \theta_{a_i} - \theta_i  < \frac{\pi}{12} \\ 0 & \text{if }  \theta_{a_i} - \theta_i  \geq \frac{\pi}{12} \end{cases}$
Skin friction	$\vec{F}_{f_i} = \frac{1}{2} \rho_w c_f (2 l w_i) (\vec{u}_i - \dot{\vec{x}}_i) \ \vec{u}_i - \dot{\vec{x}}_i\  \cos^2(\theta_{a_i} - \theta_i)$ where $c_f \approx 0.074 \text{Re}^{-\frac{1}{5}} \approx 0.02$
Hydrodynamic inertial forces	$\vec{F}_{I_i} = \rho_w l w_i b_i (\ddot{\vec{u}}_i + c_{a_i} (\ddot{\vec{u}}_i - \ddot{\vec{x}}_i))$

Although  $\vec{F}_I$  may have indirect effects by altering blade motion, the direct contribution to wave attenuation can be neglected.

Ultimately, the effects of the forces and the turbulence production are captured in  $C_D$ , which can be used in large-scale models.  $C_D$  is defined such that

$$\hat{P}_T = \frac{1}{T} \int_0^T \int_0^L \frac{1}{2} \rho_w C_D w |u|^3 dz dt \quad (9)$$

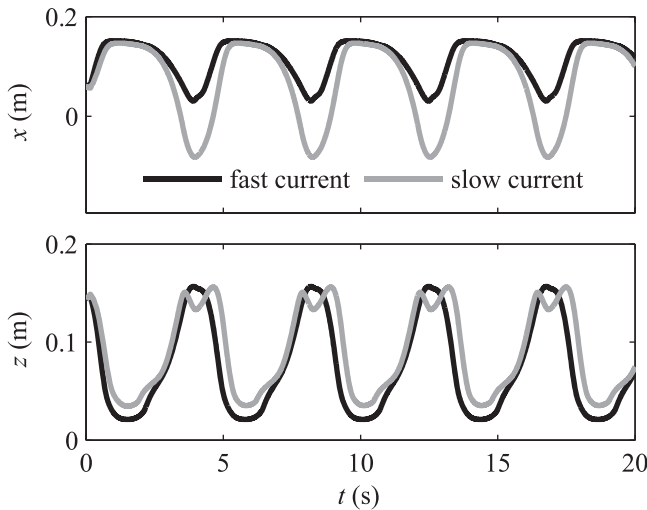


Fig. 2. Example of numerical blade-tip location as a function of time. Results are shown for the 0.25 mm thick, 15 cm long blade in the Medium waves at both the Fast and Slow pump settings.

where  $w$  is the blade width,  $u$  is the phase-averaged streamwise fluid velocity,  $z$  is the vertical dimension, and  $t$  is time.  $C_D$  is computed by rearranging Eq. 9 to solve for  $C_D$ . All other terms in Eq. 9 can be computed using the present numerical model. Equation 9 can be rewritten to use wave attenuation rather than  $\hat{P}_T$  in order to apply measurements from the field or laboratory, where  $\hat{P}_T$  is difficult to measure directly. The method of computing  $C_D$  by using Eq. 9 is based on Dalrymple et al. (1984). However, Dalrymple et al. (1984) assumed linear wave theory to get the velocity  $u$ , whereas the present study used phase-averaged velocity measurements from the laboratory.

*Laboratory experiments*—Experiments were conducted in the Stanford Environmental Fluid Mechanics Laboratory recirculating wave flume, which is 6.9 m long with a 4.9 m long  $\times$  1.2 m wide test section (see Fig. 3). Additional details of the flume assembly can be found in Weitzman (2013). A variety of waves were produced with a plunging-type wavemaker.  $T$  varied between 2.62 s and 5.19 s,  $U_w$  varied between 9.45 cm s $^{-1}$  and 25.8 cm s $^{-1}$ , and  $A_{\text{rms}}^\infty$  varied between 2.75 cm and 15.2 cm. The water depth in the absence of waves was 40 cm. Fluid velocities were measured with a Nortek Vectrino acoustic velocimeter sampling at 100 Hz in order to get phase-averaged statistics. The velocimeter was mounted on a Cartesian robot, allowing transverse and vertical movements with an accuracy of 1 mm. Four wavemaker settings (‘Large,’ ‘Medium,’ ‘Small,’ and ‘None’) and two pump rates (‘Fast’ and ‘Slow’) were used to create the eight flow conditions that were used for model validation. In the absence of waves, the Fast current had a freestream time-averaged streamwise

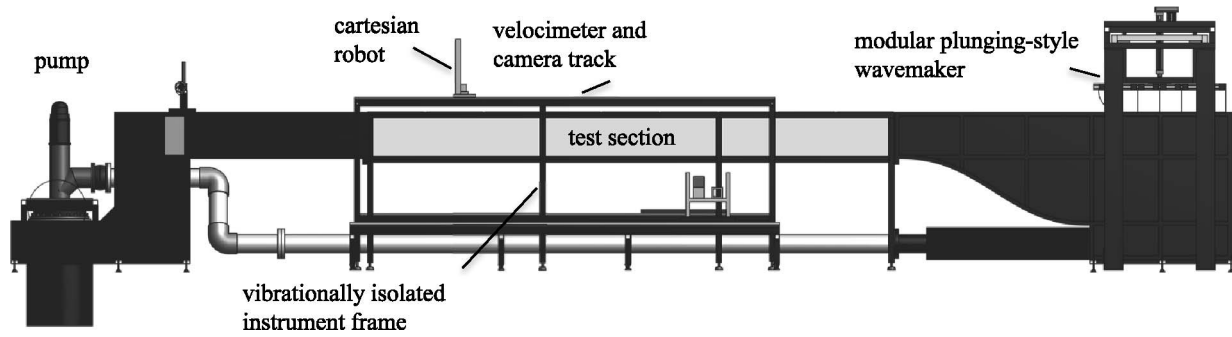


Fig. 3. Flume schematic.

velocity,  $U_c$ , of  $13.7 \text{ cm s}^{-1}$  and the Slow current had a  $U_c$  of  $3.66 \text{ cm s}^{-1}$ . The flow conditions for the validation experiments are summarized in Table 2. Figure 4 gives phase-averaged streamwise velocities for all four wave types at the Fast pump rate. For the model validation cases, the flow was measured at eight heights for 6 min each. Eighteen additional wave conditions, designated ‘A’ through ‘R’ were measured to generate more inputs for the model. For these waves, the velocity was measured at a single height in the freestream for 6 min with the Fast pump rate. The wave parameters for A through R span the range between the Small and Large waves. In order to vary the relative magnitude of the wave and current velocities for the numerical model, the mean velocity profile was multiplied by a scalar value. Ten different values were used for each of the 18 wave conditions, leading to 180 conditions for the numerical model runs. The additional flow conditions for the numerical model runs are summarized in Table 3.

For the validation experiments, four model blades with different properties were created in order to vary  $\lambda_R$  independently of the flow conditions. Each model blade consisted of a strip of low-density polyethylene (LDPE) glued into a slit in a wood dowel peg of 6.4 mm diameter. Polycarbonate plates with predrilled holes were placed at the bottom of the flume test section. For any given experiment, one of the model blades was attached to the bottom by placing the wood dowel peg in one of the predrilled holes. All four blades were 1 cm wide. Three of the blades were 15 cm long with thicknesses of 0.20, 0.25, and 0.30 mm. The fourth blade was 20 cm long with a thickness of 0.25 mm. A picture of three of the model

Table 2. Flow conditions for validation experiments. Representative mean statistics from the 8 flow conditions used for the 32 laboratory and numerical validation experiments are provided.

Current	Wave	$T$ (s)	$A_{\text{rms}}^{\infty}$ (cm)	$U_w$ (cm s $^{-1}$ )	$U_c$ (cm s $^{-1}$ )
Fast	Large	5.19	15.2	25.8	12.1
	Medium	4.29	8.18	17.3	13.2
	Small	2.80	2.75	9.45	12.9
	None	—	—	—	13.7
Slow	Large	5.19	15.1	24.4	6.00
	Medium	4.29	7.86	15.9	5.63
	Small	2.80	2.75	9.64	4.77
	None	—	—	—	3.66

blades is shown in Fig. 5. LDPE has a Young’s modulus of 0.3 GPa (Ghisalberti 2005). These parameters were chosen to match field conditions with laboratory conditions based on three non-dimensional parameters that compare rigidity, buoyancy, and hydrodynamic inertial forces to drag. The rigidity parameter,  $\lambda_R$ , is defined in Eq. 1. The buoyancy and hydrodynamic inertia parameters are denoted  $\lambda_B$  and  $\lambda_I$ , respectively:

$$\lambda_B = \left( \frac{\rho_g}{\rho_w} - 1 \right) \frac{bg}{U_{\text{max}}^2}; \quad \lambda_I = \frac{b\dot{U}}{U_{\text{max}}^2} \quad (10)$$

where  $\rho_g$  is the density of the blade,  $g$  is the gravitational acceleration, and  $\dot{U}$  is the characteristic streamwise fluid acceleration. All three parameters,  $\lambda_R$ ,  $\lambda_B$ , and  $\lambda_I$ , vary by multiple orders of magnitude in the field, and the parameters for the laboratory models fall within a realistic range for *Thalassia testudinum*. This species of seagrass was chosen because the elements are relatively rigid, but still exhibit large deflections. Meadows of *Thalassia testudinum* have been used for previous field studies of  $KC$  param-

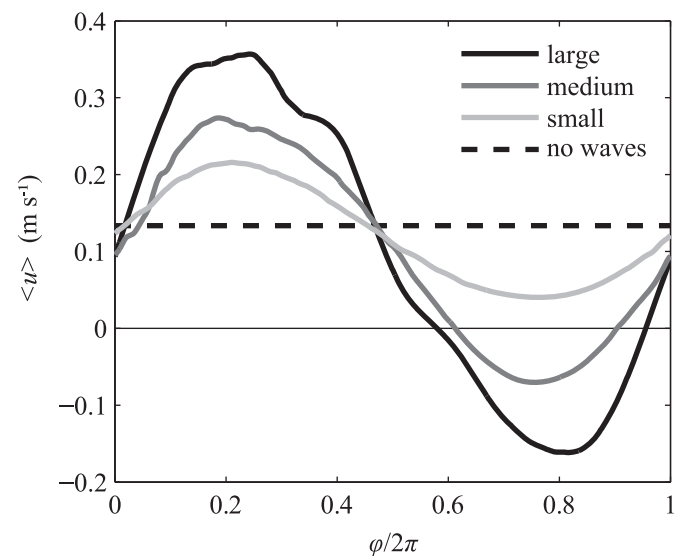


Fig. 4. Example phase-averaged velocities as a function of wave phase. Measurements are from  $z = 13.2 \text{ cm}$  above the bed and the pump rate was at the Fast setting. This height was chosen because the velocities are approximately what the model blades experienced.

Table 3. Flow conditions for numerical model runs. Representative mean statistics are provided for the additional 180 flow conditions that were used to force the model in developing the method of predicting wave attenuation. The wave statistics for the 18 laboratory waves were measured at a single height while the pump was at the Fast rate. The currents are artificial and were computed by scaling the mean velocity profile for the Fast current with no waves. The flow conditions used in the model runs are the superposition of the wave and current velocities.

Waves (measured in Fast current)			
Name	$T$ (s)	$A_{rms}^{\infty}$ (cm)	$U_w$ (cm s <sup>-1</sup> )
A	4.87	16.4	21.2
B	5.11	17.5	23.2
C	4.76	15.9	20.9
D	4.64	15.4	20.7
E	4.38	14.2	20.2
F	4.16	13.1	19.0
G	4.15	12.6	19.2
H	4.82	14.8	18.1
I	4.51	13.7	17.8
J	4.22	12.3	15.9
K	3.91	10.6	16.2
L	3.61	9.42	13.1
M	3.31	8.82	14.4
N	3.02	8.13	16.2
O	2.71	7.08	14.5
P	2.42	6.06	14.0
Q	2.59	6.43	11.4
R	2.62	6.38	10.6

Currents (artificial)			
Name	$U_c$ (cm s <sup>-1</sup> )		
1	2.74	—	—
2	5.48	—	—
3	8.22	—	—
4	11.0	—	—
5	13.7	—	—
6	16.4	—	—
7	19.2	—	—
8	21.9	—	—
9	24.7	—	—
10	27.4	—	—

terization and wave attenuation in flexible vegetation (Bradley and Houser 2009; Weitzman et al. 2013). It is also the dominant species of seagrass in the tropical Atlantic (Short et al. 2007).

Blade flexural response was imaged at 30 frames s<sup>-1</sup> using a side-facing digital video camera with a resolution of 1920 × 1080 pixels. Ten minutes of video were acquired for each of the four blades in each of the eight flow conditions. The blades were colored black and backlit in order to maximize contrast. An algorithm using MATLAB's image processing toolbox was used to identify the position of the blade in each frame, specifically the blade-tip location. The images in Fig. 6 exemplify the processing steps. The scale of the image was calibrated by taking images of a plastic cylinder of known width. The processing algorithm typically identified the blade-tip location within 1 mm of where it

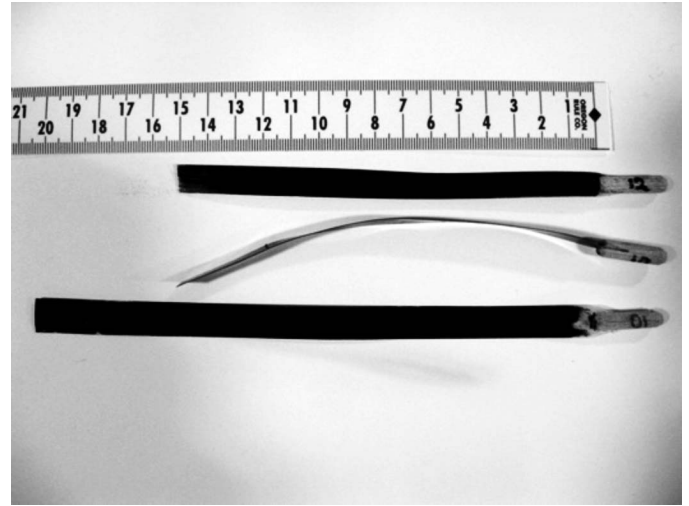


Fig. 5. Picture of laboratory model blades. From top to bottom, the blades are 0.30 mm thick, 15 cm long; 0.25 mm thick, 15 cm long; and 0.25 mm thick, 20 cm long. The middle blade has been laid on its side to show the slit in the wood dowel where the plastic strip is attached.

would be placed by eye. At times, the blade twisted, causing portions of the blade to disappear in the image. Although the image of the blade could typically be reconstructed to identify the tip, it occasionally resulted in spurious data points that had to be removed. The image of the blade was clearest when the blade was pronated and when the tip reached its horizontal extents, which are the only positions that were used quantitatively in this study. In general, the variance in the blade-tip location for a particular wave phase was at least one order of magnitude larger than the error due to the quantitative imaging methods. The resulting time series of ~ 18,000 blade-tip positions for each scenario was used for comparison with the numerical results.

## Results

The results in this paper are reported in six subsections. (1) The laboratory model blade deflections are compared with previous results in the literature to ensure that the behavior is consistent with the prototype. (2) The numerical and laboratory results are compared in order to validate the numerical model. (3) Collapse of the model data onto a  $C_D$ - $KC_{BBE}$  curve demonstrates that  $L_{BBE}$  is an appropriate length scale to use in  $KC$  for a flexible blade. (4) The qualitative observations and reasoning that led to the algebraic model for predicting wave attenuation are presented. (5) The quantitative relationships that underlie the algebraic model are described in detail. (6) The algebraic model is compared with previous parameterizations.

*Laboratory model validation*—The deflections of the laboratory model blades were consistent with results from the literature. Figure 7 shows the non-dimensional pronated height of the blade tip,  $z_{pro}^* = z_{pro}L^{-1}$ , as a function of  $U_{max}$ . For wavy cases,  $z_{pro}$  is defined as the  $z$ -position of the blade tip when the  $x$ -position is at its maximum value over

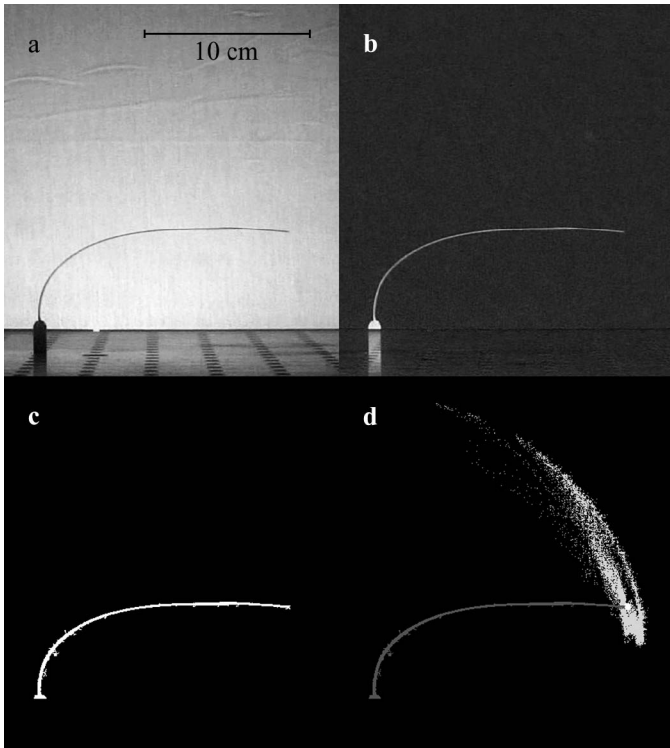


Fig. 6. Illustration of image processing steps: (a) raw image of the blade silhouette; (b) inverted image with the background removed; (c) binary image generated by adaptive thresholding and removal of objects with area  $< 200$  pixels; (d) tip location identified for the current frame (white circle) and tip locations for the full 18,000 video frames (gray dots).

the wave period. For cases without waves,  $z_{\text{pro}}^*$  is the  $z$ -position of the blade tip and  $U_{\text{max}} = U_c$ . In Fig. 7, results from the present study are compared with those of Fonseca and Kenworthy (1987) and Luhar and Nepf (2011). The data from Fonseca and Kenworthy (1987) are for a meadow of *Thalassia testudinum* exposed to a unidirectional current in a laboratory flume. The data from Luhar and Nepf (2011) are numerical model predictions for a single blade exposed to a unidirectional current. Although the  $z_{\text{pro}}^*$  values for the present study fall below those of Fonseca and Kenworthy (1987), they follow the low-rigidity bound from Luhar and Nepf (2011). The blade motion is more chaotic and more difficult to model when the blades are more flexible. Validation in this region of parameter space ensures that the model is robust enough to handle more complex behavior.

It should also be noted that the differences between the results from the present laboratory model and results from the natural grass from Fonseca and Kenworthy (1987) are partially due to the experimental conditions and not necessarily differences in the blade rigidity. The present study used a single blade, rather than a full meadow. Without sheltering from a surrounding meadow, the blade deflections are larger, resulting in decreased  $z_{\text{pro}}^*$ . The present study included waves. Because  $z_{\text{pro}}^*$  is defined in wavy cases at the precise moment that the blade is most deflected, results from wavy cases contain a bias toward

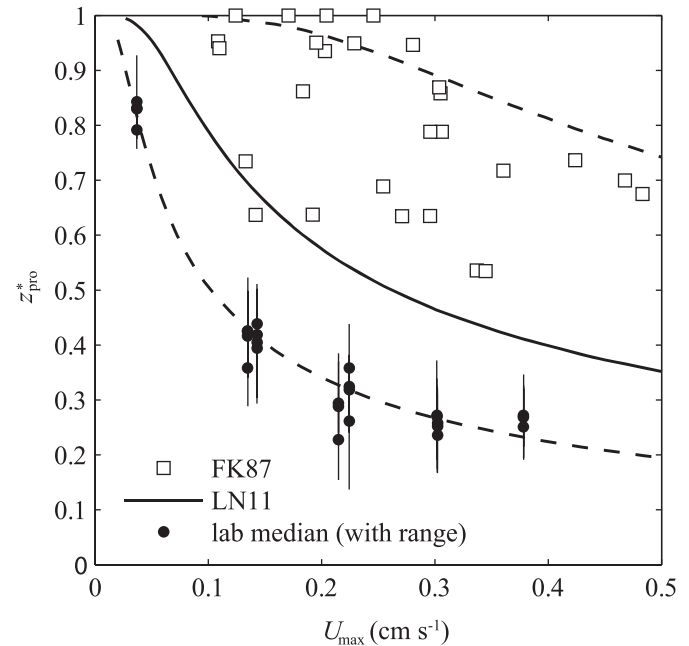


Fig. 7.  $z_{\text{pro}}^*$  vs.  $U_{\text{max}}$  from the laboratory model compared with results from previous studies. The data labeled ‘FK87’ are from flume measurements with a real seagrass meadow in unidirectional flow (Fonseca and Kenworthy 1987). The data labeled ‘LN11’ are from a numerical model of a single blade in a unidirectional flow (Luhar and Nepf 2011). All three studies were based on *Thalassia testudinum*. The three lines for LN11 represent three cases with different rigidities. From bottom to top, they are a low rigidity bound, a typical rigidity case, and a high rigidity bound. The data from the present study are given as a median and a range of  $z_{\text{pro}}^*$  for each run.

smaller  $z_{\text{pro}}^*$ . Results from unidirectional cases do not contain this bias.

**Numerical model validation**—The laboratory and numerical results demonstrate reasonable agreement for blade-tip location and show similar trends for pronated height as a function of rigidity. In Fig. 8, every sampled blade-tip location is plotted to compare numerical and laboratory results from individual experiments. The two subplots correspond to two separate experiments—one where the laboratory results were relatively consistent over each wave (Fig. 8a), and one where the laboratory blade motion was chaotic (Fig. 8b), causing inaccuracies in the blade-tip identification. Although the results for chaotic motion show much more scatter, the numerical and laboratory results are consistently in agreement when the blade is pronated. Later, pronated height is shown to be the critical aspect of the blade motion, suggesting that the results are accurate during the most important part of the wave period. Figure 9 shows  $z_{\text{pro}}^*$  as a function of  $\lambda_R$ . Both laboratory and numerical results are presented in order to compare trends over all experiments. For the laboratory data, the median values are plotted along with the range within two standard deviations of the mean ( $\mu \pm 2\sigma$ ) and the range within the minimum and maximum values in order to quantify the variability. The five laboratory values

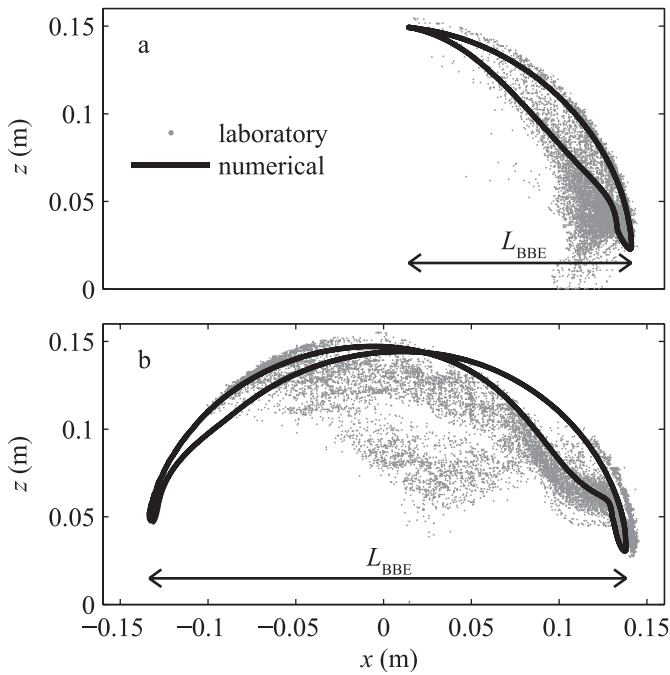


Fig. 8. Example comparisons of laboratory and model results for blade tip orbital: (a) 0.25 mm thick, 15 cm long blade in Medium waves at the Fast pump rate; and (b) 0.30 mm thick, 15 cm long blade in Large waves at the Slow pump rate. The arrows show  $L_{BBE}$  for the numerical results.

with no corresponding numerical value are the cases in which the numerical solution did not converge. The numerical  $z_{pro}^*$  values typically fall within the range of laboratory observations and many of the results are within the  $\mu \pm 2\sigma$  range. The numerical model also reproduces the trend that blades with higher rigidity pronate less, such that  $z_{pro}^*$  increases with  $\lambda_R$ . The location and slope of this transition are similar in the numerical and laboratory results. Although there is some disagreement in the value of  $z_{pro}^*$  for specific runs, these typically occur at extreme values of  $\lambda_R$ . This may be attributed to imperfections in the laboratory models: the blade pronation is limited by the attachment of the LDPE strips to the wood dowel pegs (relevant at low  $\lambda_R$ ) and natural curling of the LDPE strips is more influential when the flow is weak (at high  $\lambda_R$ ). However, the overall agreement between the numerical and laboratory results is satisfactory for a study that seeks to identify the best physical characteristics for parameterizing a complex system.

Discrepancies in the two results can be attributed to a number of physical peculiarities of the grass mimics that were not accounted for in the numerical model. (1) The strips of LDPE had a slight preference for curling on one side as soon as they were cut, and it is hypothesized that there was some hysteresis in the bending of the strips due to prolonged exposure to currents. (2) The attachment of the strips to the wood dowel pegs was found to increase the rigidity at the bottom of the strip due to slight curvature. (3) Only the ensemble-averaged flow was applied in the model. Although turbulent fluctuations had little effect on the pronated position of the blade, they did cause

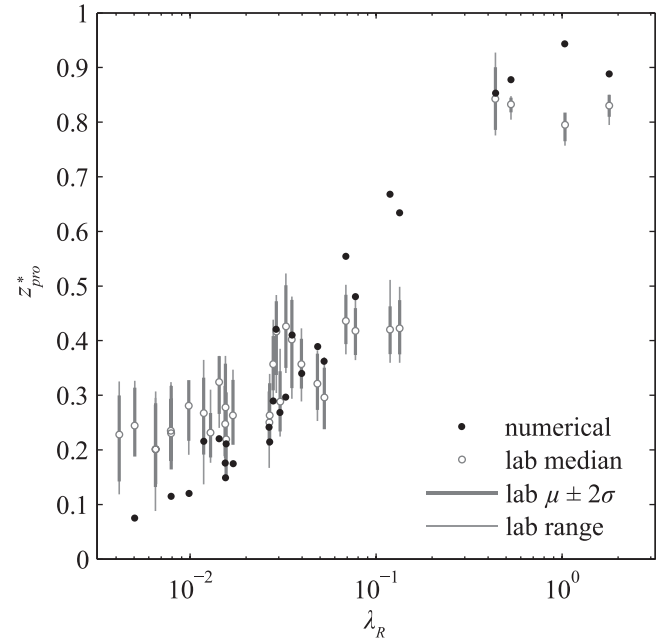


Fig. 9. Comparison of laboratory and numerical model results for non-dimensional pronated blade-tip height,  $z_{pro}^*$ , as a function of  $\lambda_R$ . In order to quantify the variability in the laboratory results, their distributions are represented by the median, the range within two standard deviations of the mean, and the full range of observed values.

significant variability in the path that the blade took during backward motion. Because the fluid velocities are relatively small during this wave phase, these motions are expected to have little effect on turbulence production. (4) Although the image processing accurately identified the blade tip when it was pronated, the twisting of the blade during backward motion decreased the accuracy of the blade detection. This accounts for much of the scatter in the blade-tip location results. The scatter due to turbulent fluctuations and imperfect blade-tip detection are exemplified in Fig. 8b. Note that the numerical model predictions of the pronated position of the blade tip, which is the most important property of the blade motion, are still in excellent agreement with the results from the laboratory models.

All of the attributes described above are likely found in real seagrass blades. Many of them can be accounted for in the present model by adjusting individual blade segment parameters, such as spring constant, undisturbed torsion spring angle, and spatial dimensions. However, quantifying these complexities in the field and applying them in the model would require prohibitively detailed and extensive measurements of seagrass biomechanical properties. In this study, the numerical blade properties were varied for a series of additional model runs in order to mimic curling of the plastic strip, hysteresis, and increased rigidity at the base. Although these changes caused the results to vary, the same trend in pronated height held true in all cases. Therefore, peculiarities of the blade properties will be ignored going forward, and parameterization conclusions will be based on trends in the numerical results.

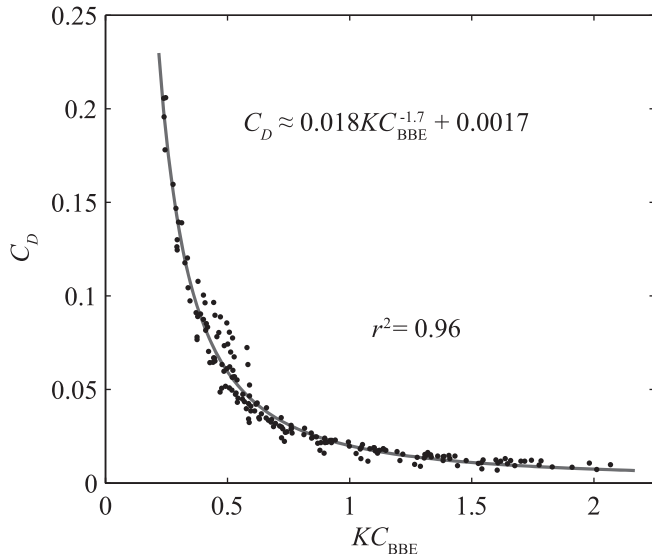


Fig. 10. Numerical model results for  $C_D$  as a function of  $KC_{BBE}$  along with a power-law fit. The accuracy of the fit is quantified by the coefficient of determination,  $r^2$ .

The collapse of the  $z_{\text{pro}}^* - \lambda_R$  data confirms that  $\lambda_R$  captures the key force balance that determines frontal area of a seagrass blade exposed to waves. Data points with similar values of  $\lambda_R$ , but different values of the dimensional parameters ( $U_{\text{max}}$ ,  $L$ , and  $b$ ), demonstrated spread that was similar to the spread in data points from the same experimental conditions. For the results in the remainder of this paper,  $\lambda_R$  was varied only through changes in  $U_{\text{max}}$ .

*Keulegan-Carpenter number based on blade bending*—The results in Fig. 10 show that  $KC_{BBE}$  is an excellent predictor of  $C_D$ . The coefficient of determination is  $r^2 = 0.96$ . The data points were computed from the 180 numerical model runs and the fit is a simple power law. Physically, any form of  $KC$  represents how much the flow develops over a wave period. In this case, the development is indicated by the degree of bending of the blade. When  $KC_{BBE}$  is large, the blade pronates early in the wave phase, reducing the frontal area when the fluid velocity is highest. When  $KC_{BBE}$  is small, the blade adjustment is long relative to the wave period, such that the fluid encounters much more of the blade's frontal area. Because frontal area effectively determines  $C_D$ , the inverse relationship between  $C_D$  and  $KC_{BBE}$  becomes apparent.

Because  $KC_{BBE}$  accounts for bending, the fitting parameters are independent of vegetation parameters, and data from any site should collapse onto a single  $C_D - KC_{BBE}$  curve. Unfortunately, the  $C_D - KC_{BBE}$  relationship is not a practical tool for predicting wave attenuation. This is because  $L_{BBE}$  would have to be measured through image acquisition, or estimated by measuring blade parameters and modeling the blade motion. Empirically adjusting models to specific sites is more practical because wave attenuation is easier to measure than blade parameters. However, the collapse of the  $C_D - KC_{BBE}$  data emphasizes what is missing from previous versions of  $KC$  and  $Re$ ; no parameter can properly non-dimensionalize the system without accounting for blade

motion. For flexible vegetation, the use of blade width in  $KC$  and  $Re$  provides little value and is simply a vestige of canonical parameterizations.

*Summary of observations used in the algebraic model development*—Although seagrass blade motion under waves is a complex nonlinear process, laboratory and numerical observations from the present study suggest that aspects of the behavior that influence wave attenuation are relatively simple and predictable. The proposed algebraic model is based on these observations.

Over the period of a wave, a seagrass blade moves freely with the flow until it reaches a maximum extent and becomes pronated. Although blade dynamics can be chaotic during the free motion, the specifics have little influence on the total turbulence production due to the low relative velocities. Once the blade becomes pronated, the relative velocities increase dramatically. The majority of the turbulence production occurs in this orientation. The proposed algebraic model hinges on the result that total turbulence production over the wave period is dominated by phases in which the blade is pronated. It is logical that most of the turbulence production occurs in a small portion of the wave period because it scales with velocity cubed.

While the blade is pronated, the position of the blade is predictable and the shape of the turbulence production curve is consistent across all model runs (see Fig. 11a). The blade is typically pronated during the first 60% of the wave period, and the turbulence production during this time can be accurately predicted by  $U_{\text{max}}$ . The turbulence production during the first 60% of the wave period is much higher than average, and typically accounts for 85–95% percent of the total turbulence production. Therefore,  $U_{\text{max}}$  alone can give a rough estimate of the total turbulence production.

To improve the turbulence production estimate, the proportionality between the turbulence production during the first 60% of the wave and the total turbulence production must be estimated. This proportionality is strongly affected by changes in the relative strength of the waves and the current. Qualitative observations of the blade motion explain this dependence. When the current dominates, the blade remains pronated for the entire wave period. When the waves dominate, the strong wave reversal causes the blade to deflect in the upstream direction to the point where blade motion is arrested. When the wave and current velocities are approximately equal, the blade moves freely with the flow after the first 60% of the wave. These kinematic observations suggest that the relative velocity after the first 60% of the wave period is dependent on the relative magnitude of the waves and current, with a minimum when they are about equal. The result is that the ratio between the turbulence production during the first 60% of the wave period, and the total turbulence production is well-predicted by a parameter that compares the waves and the current.

By developing quantitative relationships based on the observations above, the total turbulence production,  $\hat{P}_T$ , can be predicted from simple parameters.

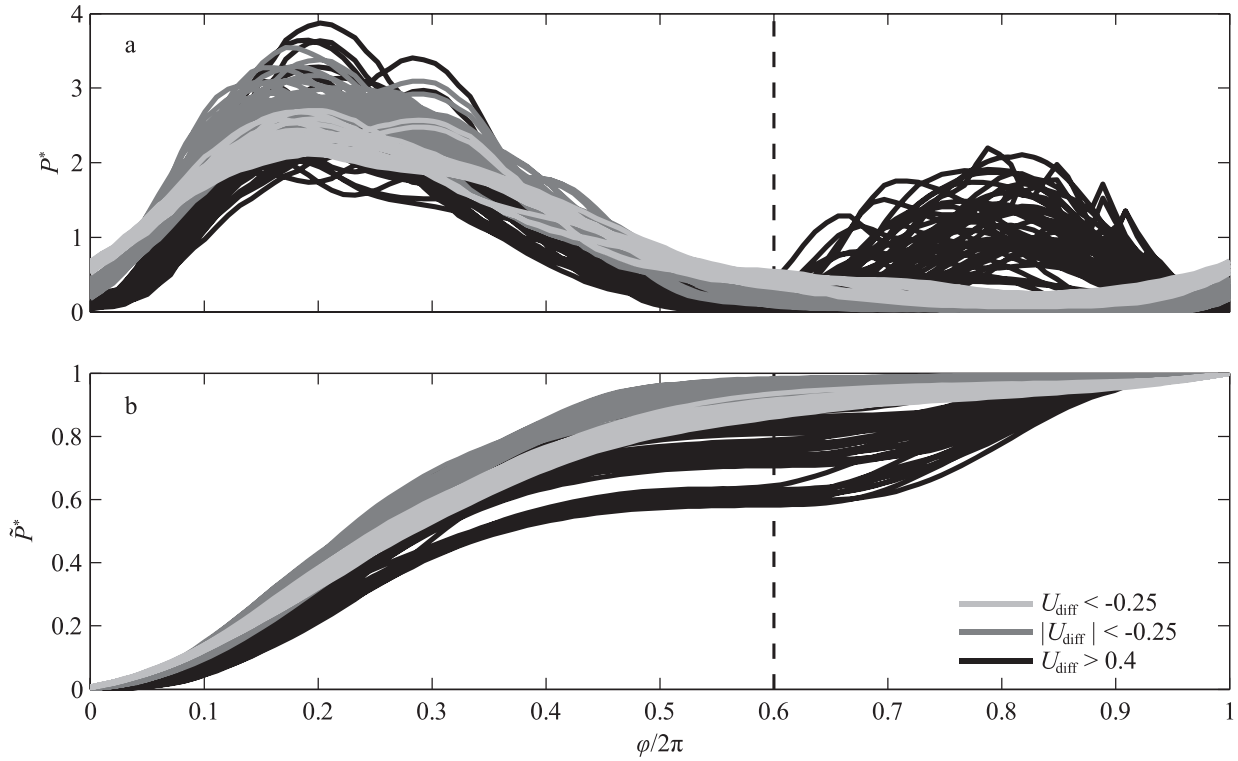


Fig. 11. Numerical model results for depth-integrated turbulence production as a function of wave phase: (a) instantaneous depth-integrated turbulence production normalized by the average turbulence production over the wave phase,  $P^*$ ; (b) cumulative depth-integrated turbulence production normalized by the total turbulence production over the wave phase,  $\tilde{P}^*$ . The vertical lines mark  $\phi/2\pi = 0.6$ .  $\tilde{P}_{60}^*$  is given by the value in plot (b) at this phase.

*Development of the algebraic model for predicting turbulence production*—The quantitative relationships that support the proposed algebraic model are presented below.

(a) During the portion of the wave period when the blade is pronated, turbulence production demonstrates consistent behavior as a function of wave phase and turbulence production during this time dominates the total turbulence production over the wave period. Turbulence production by the blade wake was estimated by taking the dot product of the velocity with the drag force, as described in the methods section. In Fig. 11a,  $P$  is non-dimensionalized by the average turbulence production over the wave period:

$$P^*(\phi) \equiv \frac{P(\phi)}{\hat{P}_T} \quad (11)$$

The phase-dependent turbulence production demonstrates a consistent shape over all waves and currents sampled. During the forward motion of the wave orbital velocity, the blade initially moves with the fluid. It then becomes pronated and the relative velocity approaches the fluid velocity. The maximum turbulence production occurs just before  $\phi/2\pi = 0.25$ , where the maximum streamwise wave velocity occurs (see Fig. 4). As the streamwise wave velocity decreases, turbulence production decreases and almost reaches zero by the time the streamwise wave velocity is zero, near  $\phi/2\pi = 0.5$ . After 60% of the wave period has elapsed ( $\phi/2\pi = 0.6$ ), there is relatively little turbulence production. (The three different cases for  $U_{\text{diff}}$

shown in Fig. 11 are discussed in more detail in ‘c’ below.) The non-dimensional, depth-integrated, cumulative turbulence production is defined as

$$\tilde{P}^*(\phi) \equiv \frac{\int_0^\phi P(\hat{\phi}) d\hat{\phi}}{\hat{P}_T} \quad (12)$$

where  $\tilde{P}_T = T\hat{P}_T$  is the total depth-integrated turbulence production over the wave period. The values of  $\tilde{P}^*$  in Fig. 11b suggest that between 60% and 100% of the turbulence production occurs before  $\phi/2\pi = 0.6$ . The value of  $\tilde{P}^*$  at this phase represents the fraction of the total turbulence production that occurs during the first 60% of the wave period and is denoted  $\tilde{P}_{60}^*$ :

$$\tilde{P}_{60}^* \equiv \frac{\int_0^{0.6(2\pi)} P(\hat{\phi}) d\hat{\phi}}{\hat{P}_T} \quad (13)$$

(b) Because the dynamics of the system are relatively simple when the blade is pronated, the associated turbulence production can be accurately predicted by the rigidity parameter and the maximum fluid velocity. Here it is assumed that the blade is pronated for the initial 60% of the wave. The total turbulence production for this time is denoted  $\tilde{P}_{60}$ ,

$$\tilde{P}_{60} \equiv \int_0^{0.6(2\pi)} P(\hat{\phi}) d\hat{\phi} \quad (14)$$

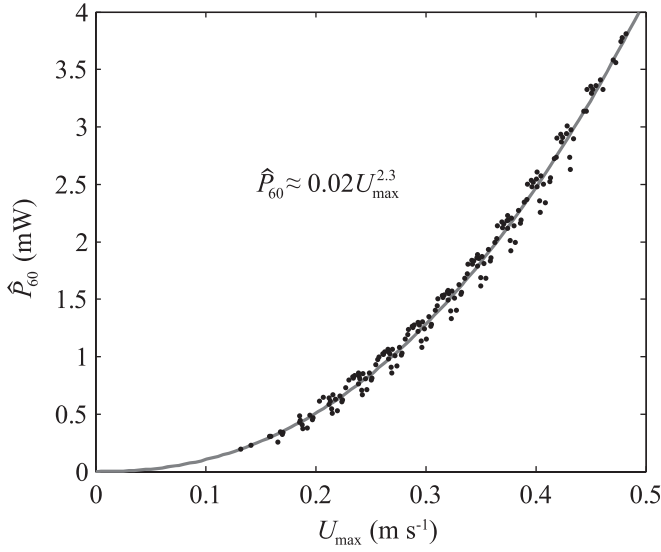


Fig. 12.  $\hat{P}_{60}$  as a function of  $U_{\max}$ . Numerical model results are shown as black dots. The gray fit line is a power-law function derived from the fitting parameters in Eq. 24.

and the average is denoted  $\hat{P}_{60}$ ,

$$\hat{P}_{60} \equiv \frac{1}{0.6T} \int_0^{0.6(2\pi)} P(\hat{\phi}) d\hat{\phi} \quad (15)$$

$\hat{P}_{60}$  is primarily dependent on the frontal area of the blade and the velocity of the fluid because the pronated blade is essentially stationary. The frontal area is determined by  $\lambda_R$ . Figure 9 gives laboratory and numerical results for  $z_{\text{pro}}^*$ , which determines frontal area when the blade is pronated, as a function of  $\lambda_R$ .  $\hat{P}_{60}$  can be written in terms of an effective drag coefficient,  $C_D^{60}$ , and  $U_{\max}$ , which is appropriate because the maximum fluid velocity will dominate turbulence production:

$$\hat{P}_{60} = \frac{1}{2} \rho_w w L C_D^{60} U_{\max}^3 \quad (16)$$

$C_D^{60}$  is assumed to be a power-law function of  $\lambda_R$ , which determines both the frontal area and the angle of the blade:

$$C_D^{60} = f(\lambda_R) \propto \left( \frac{Eb^3}{\rho_w L^3 U_{\max}^2} \right)^\alpha \quad (17)$$

where  $\alpha$  is a constant. Substituting back into the expression for  $\hat{P}_{60}$  gives

$$\hat{P}_{60} \propto \frac{1}{2} \rho_w w L \left( \frac{Eb^3}{\rho_w L^3} \right)^\alpha U_{\max}^{3-2\alpha} \quad (18)$$

For a fixed set of blade parameters, as in the model runs, this can be simplified to a power law:

$$\hat{P}_{60} = C U_{\max}^\gamma \quad (19)$$

where  $C$  and  $\gamma$  are constants that are ultimately incorporated into fitting parameters. Note that  $C$  accounts for the dependence on blade parameters:  $C \propto \frac{1}{2} \rho_w w L \left( \frac{Eb^3}{\rho_w L^3} \right)^\alpha$ . The

$\hat{P}_{60}$  data are shown in Fig. 12 along with the predicted values from the fit.

(c) The mechanism and behavior of turbulence production when the blade is not pronated depends on the relative strength of the waves and current. The wave and current velocity are compared using the non-dimensional parameter  $U_{\text{diff}} \equiv (U_w - U_c)(U_w + U_c)^{-1}$ , where  $U_c$  is the mean and  $U_w$  is the maximum deviation above the mean of the phase-averaged freestream streamwise velocity. Three regimes of  $U_{\text{diff}}$  give three different shapes of  $P^*$ : (1) When the wave and current velocity are close to equal ( $U_{\text{diff}} \approx 0$ ),  $P^*$  after  $\phi/2\pi = 0.6$  is near zero because the relative velocity between the blade and the fluid is extremely small. (2) When the wave dominates ( $U_{\text{diff}} > 0$ ), the flow reverses sufficiently for the blade's motion to be arrested on the reversal, leading to a second peak in  $P^*$  near  $\phi/2\pi = 0.75$ . (3) When the current dominates ( $U_{\text{diff}} < 0$ ), the streamwise velocity remains significant after  $\phi/2\pi = 0.6$ , such that the blade remains pronated, resulting in a higher baseline turbulence production. The qualitative aspects of the blade motion were observed in both laboratory and numerical experiments. The numerical results for  $P^*$  are depicted in Fig. 11a with the three regimes of  $U_{\text{diff}}$  denoted by the three shades of gray.

(d) The proportion of turbulence production that occurs while the blade is pronated is well-predicted by a comparison between the wave and current velocities. Figure 11b shows the normalized cumulative turbulence production over the wave phase,  $\tilde{P}^*$ , for the three regimes of  $U_{\text{diff}}$ . The relative contribution to turbulence production from the time when the blade is pronated,  $\tilde{P}_{60}^*$ , is seen in Fig. 11b as the value of  $\tilde{P}^*$  at  $\phi/2\pi = 0.6$ . As with  $P^*$ , the three regimes of  $U_{\text{diff}}$  give three different shapes of  $\tilde{P}^*$ : (1) When  $U_{\text{diff}} > 0$ , there is a sharp jump in  $\tilde{P}^*$  near  $\phi/2\pi = 0.75$ , which is attributed to the blade motion being arrested as the blade bends in the upstream direction (observed in both laboratory and numerical experiments). (2) When  $U_{\text{diff}} \approx 0$ , the  $\tilde{P}^*$  is above 90% by  $\phi/2\pi = 0.6$ , showing little contribution to overall turbulence production when the blade is not pronated. (3) When  $U_{\text{diff}} < 0$ , there is a significant gradual increase in  $\tilde{P}^*$  after  $\phi/2\pi = 0.6$  because the blade remains partially pronated and the background current continues to produce turbulence. These differences naturally translate to a relationship between  $\tilde{P}_{60}^*$  and  $U_{\text{diff}}$ , which is shown in Fig. 13. For the predictive method, the relationship is approximated with a parabola:

$$\tilde{P}_{60}^* = c_2 U_{\text{diff}}^2 + c_1 U_{\text{diff}} + c_0 \quad (20)$$

where  $c_2$ ,  $c_1$ , and  $c_0$  are constants that are later incorporated into fitting parameters.  $\tilde{P}_{60}^*$  is maximized near  $U_{\text{diff}} = 0$  and demonstrates the smallest variance at this location. This is because turbulence production in the early part of the wave phase is most dominant when the wave and current velocities are similar. The spread increases for  $U_{\text{diff}} > 0$  because the dominant wave velocity causes the blade motion to become more chaotic. In this sense, the current stabilizes the system. Qualitative laboratory observations suggest that seagrass blades grouped in canopies demonstrate less chaotic behavior than do individual

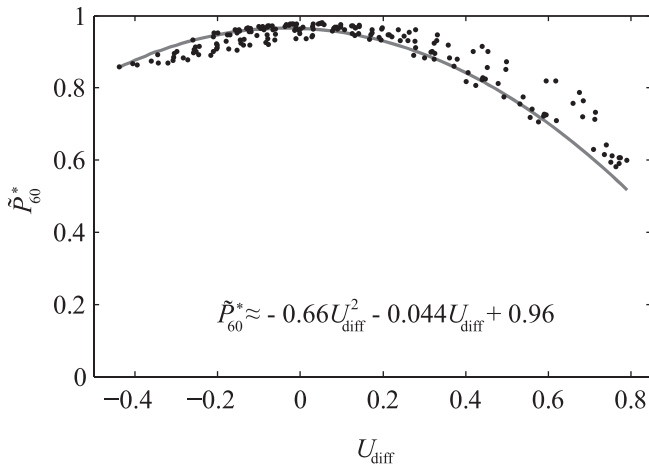


Fig. 13.  $\hat{P}_{60}^*$  as a function of  $U_{diff}$ . Numerical model results are shown as black dots. The gray line is a quadratic function derived from the fitting parameters in Eq. 24.

blades. This may improve the  $U_{diff}$  parameterization when it is applied to a canopy.

(e) By predicting turbulence production while the blade is pronated and predicting what portion of the total turbulence production occurs during this time, the total turbulence production can be estimated from simple flow parameters. The ratio of the time-averaged turbulence production values can be related to the integrated turbulence production values using their definitions (Eqs. 15, 16):

$$\frac{\hat{P}_T}{\hat{P}_{60}} = \frac{\tilde{P}_T/T}{\tilde{P}_{60}/0.6T} \quad (21)$$

This relationship can be rearranged in order to relate  $\hat{P}_T$  to  $\hat{P}_{60}^*$  and  $\tilde{P}_{60}$ :

$$\hat{P}_T = 0.6 \frac{\tilde{P}_{60}}{\hat{P}_{60}^*} \quad (22)$$

$\hat{P}_{60}$  is related to  $U_{max}$  by a power law (Eq. 20). Dependence on  $\lambda_R$  is contained in  $C$  and  $\gamma$ .  $\tilde{P}_{60}^*$  is related to  $U_{diff}$  by a quadratic polynomial (Eq. 21). Combining the two relationships gives an algebraic model for  $\hat{P}_T$ :

$$\hat{P}_T = \frac{U_{max}^\gamma}{b_2 U_{diff}^2 + b_1 U_{diff} + b_0} \quad (23)$$

where  $b_2 = c_2(0.6C)^{-1}$ ,  $b_1 = c_1(0.6C)^{-1}$ , and  $b_0 = c_0(0.6C)^{-1}$ . The units of  $b_2$ ,  $b_1$ , and  $b_0$  are  $N^{-1}m^\gamma s^{1-\gamma}$ . A non-linear fit was used to determine the fitting parameters,  $\gamma$ ,  $b_2$ ,  $b_1$ , and  $b_0$ , which are reported in Fig. 14. These are the same parameters that were used to derive the fits shown in Figs. 12, 13.  $\hat{P}_T$  was estimated for each of the 180 flow cases using the simple algebraic fit. The results are plotted against the  $\hat{P}_T$  values that were computed by the numerical blade-bending model in Fig. 14. The coefficient of determination is  $r^2 = 0.99$ . This demonstrates the accuracy of the predictive method derived in this section.

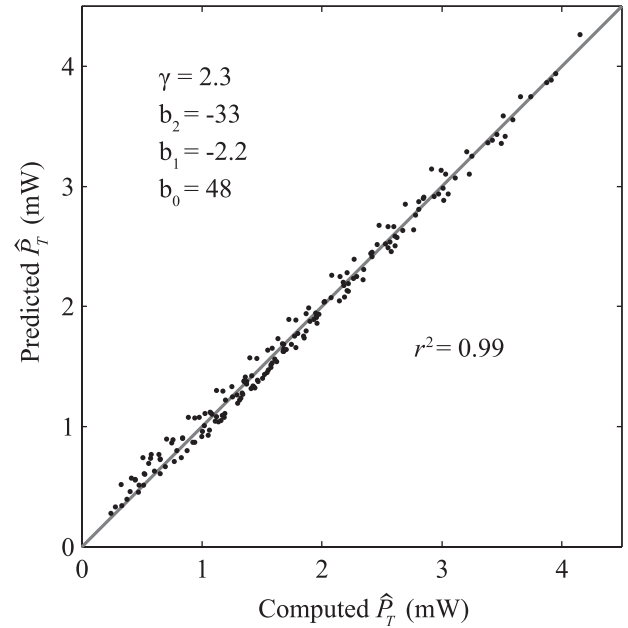


Fig. 14.  $\hat{P}_T$  predicted from the algebraic fit vs.  $\hat{P}_T$  computed from numerical model results. The gray line has a slope of 1, representing a perfect fit.

Once an estimate of  $\hat{P}_T$  is obtained, it can easily be translated to  $C_D$  according to Eq. 9. The proposed algebraic model allows  $\hat{P}_T$  and  $C_D$  to be computed from  $U_{max}$  and  $U_{diff}$ , which are both simple parameters describing the incident flow. The model must be adjusted to each specific system for which it is used because  $\lambda_R$  depends on vegetation parameters that are difficult to measure. A more detailed description of how the model would be applied is provided in the Discussion. Because the proposed algebraic model allows efficient computation of  $C_D$  from known values, it is a feasible method for accounting for drag or energy dissipation by flexible vegetation in a large-scale model.

*Connection between the algebraic model and previous parameterizations*—Under certain assumptions, a curve fit using the proposed algebraic model is equivalent to a curve fit using either the  $C_D-Re$  or the  $C_D-KC$  parameterization (Bradley and Houser 2009). Assuming fixed blade parameters and water depth, and assuming  $\hat{P}_T$  is equal to dissipation, Dalrymple et al. (1984) gives the following proportionality:  $\hat{P}_T \propto C_D \eta_0^3 k^2 \omega^{-3}$ , where  $\eta_0$  is the wave amplitude,  $k$  is the wave number, and  $\omega$  is the wave frequency. Assuming long waves,  $\omega \propto k$  and  $\eta_0 \propto U_{max}$ . Assuming that the waves have a constant slope,  $k \propto \eta_0^{-1}$ . Together, these proportionalities give  $\hat{P}_T \propto C_D U_{max}^4$ . Thus, a power-law relationship between  $C_D$  and  $U_{max}$  can be equivalently rewritten as a power law relating  $\hat{P}_T$  to  $U_{max}$ . Assuming that  $U_{max}$  is the characteristic velocity used in  $Re$ , and assuming that blade width and fluid viscosity are fixed, a  $C_D-Re$  power law is equivalent to a  $\hat{P}_T-U_{max}$  power law. Similar logic can be used to show that a  $C_D-KC$  power law is also equivalent to a  $\hat{P}_T-U_{max}$  power law. In the proposed algebraic model,  $U_{diff} = 1$  when  $U_c = 0$ .

Therefore, for fixed blade parameters in pure oscillatory flow, the algebraic model reduces to a power-law relationship between  $\hat{P}_T$  and  $U_{\max}$ .

The above logic demonstrates that under certain assumptions, the proposed algebraic model, a  $C_D$ - $Re$  power law, and a  $C_D$ - $KC$  power law can all be reduced to an equivalent relationship. This is the reason that the data presented in Bradley and Houser (2009) show nearly identical distributions and  $r^2$  values for the  $C_D$ - $Re$  and the  $C_D$ - $KC$  relationships. The fact that the proposed algebraic model reduces to previous relationships in pure oscillatory flow suggests that the parameterization is valid for field conditions. Field validation in systems with a background current would require additional experiments. The proposed algebraic model contains three significant advancements in parameterizing vegetative wave attenuation: (1) the underlying relationships are connected to physical processes that are elucidated in this text; (2) it utilizes only the essential physical parameters; and (3) it can be applied to systems that include a background current.

## Discussion

The attenuation of waves by seagrass meadows is a complex process involving the coupled dynamics of fluid and blade motion. Further complexity is introduced by variation in blade morphology, canopy heterogeneity, bottom topography, etc. Considering these uncertainties in boundary conditions, even direct numerical simulation could not provide definitive results. This leads to a reliance on empirical models for predicting wave attenuation from large-scale model parameters. However, it is not obvious which parameters would create the most effective empirical models because it is unclear how they influence the processes that eventually lead to dissipation of wave energy. A simple numerical model of blade dynamics was used to elucidate the basic processes that dominate wave attenuation by flexible elements. By determining the parameters that best characterize these processes, we have developed an understanding of how simple parameters influence the efficiency of wave attenuation. Although the proposed algebraic model is similar to previous predictive methods in pure oscillatory flow, it improves upon them with clear connections to physical mechanisms, simplicity, and applicability to complex flows.

*Seagrass as a low-pass filter*—Previous studies have compared seagrass to a low-pass filter because  $C_D$  increases with wave frequency, implying preferential attenuation of high-frequency waves (Bradley and Houser 2009). The results of this study agree, as can be seen in the decrease of  $C_D$  with increasing  $KC_{BBE}$ .  $KC_{BBE}$  is proportional to wave period, such that increased wave period (decreased wave frequency) results in lower efficiency of wave attenuation. This low-pass filtering can be caused by two different mechanisms, which occur in different frequency regimes. In the high-frequency regime, the phase lag between wave and blade motion decreases as frequency decreases because the blade has more time to react to changes in fluid velocity. In this case, changes in  $C_D$  are attributed to changes in relative

velocity. In the low-frequency regime, the blade is streamlined for a greater portion of the wave period when the frequency is lower. In this case, changes in  $C_D$  are attributed to changes in frontal area and the relative velocity actually increases with decreased frequency. Both mechanisms were alluded to in Bradley and Houser (2009). In this study, all wave periods were relatively long, such that only the low-frequency regime was observed.

*Individual blades vs. canopies*—Seagrass influences local fluid motion, a key complexity that was left out of the numerical model. Recent observations suggest that oscillatory flow and canopy flexibility both push the system toward the sparse canopy limit, in which canopy elements behave as they would individually (Lowe et al. 2005; Luhar et al. 2010). Although the blade motion and wave attenuation may not exactly mimic real seagrass in its natural environment, the mechanistic observations and the resulting parameterizations are expected to hold true for a canopy. In order to test this, the algebraic model must be tuned to field data from real seagrass meadows, allowing the fit to account for the coupling between blade and fluid motion. This validation is already available for systems with pure oscillatory flow because, in this case, the proposed algebraic model can be reduced to the  $C_D$ - $Re$  or  $C_D$ - $KC$  relationships found in the literature. Validation in systems with a background current will require additional field data, which are not currently available. In the paragraphs below, the expected effects of scaling up to a canopy and methods of accounting for these effects are discussed in more detail.

Mean current is greatly affected by meadows of sufficient density (Nepf 2012). However, wave velocities are often influenced to a much smaller degree (Luhar et al. 2013). Lowe et al. (2005) suggests that attenuation in rigid canopies is dependent on a form of  $KC$  based on element spacing. In a flexible canopy, element spacing is not the largest length scale associated with flow development. Instead,  $L_{BBE}$  may be more appropriate for predicting attenuation of orbital velocities with depth. This idea is supported by our result that  $KC_{BBE}$  is an excellent predictor of  $C_D$  for a single element. The increase in length scale that is implied by using  $L_{BBE}$  rather than canopy spacing suggests that the orbital excursion required to cause significant attenuation of orbital velocity is much larger in flexible canopies than in rigid canopies. This implies that the assumption of decoupling between blade bending and fluid motion is valid over a larger range of orbital excursions. A related conclusion is that flexible canopies attenuate orbital velocity less than rigid canopies of the same density (Peterson et al. 2004). This topic deserves further exploration, especially at higher orbital excursions, where varying  $KC_{BBE}$  is hypothesized to have a more significant effect on attenuation.

Despite the observations described above, the aggregate behavior of a canopy is certainly different from a superposition of individual blades. Here, these differences are discussed in terms of their effect on the proposed algebraic model. The most significant difference between an individual blade and a canopy is the velocity reduction

inside the canopy. This causes an increase in effective rigidity and a decrease in the forces experienced on a per blade basis. In the algebraic model, the higher effective rigidity would result in decreased  $\gamma$  because of reduced dependence of frontal area on velocity. It would also result in higher values of  $b_0$ ,  $b_1$ , and  $b_2$ , because of increased frontal area. However, the decreased forces would counteract the increased frontal area and push toward lower values of  $b_0$ ,  $b_1$ , and  $b_2$ . Another phenomenon that only appears in a canopy is physical blade–blade interaction. This would increase effective rigidity, thereby increasing  $\gamma$  and decreasing  $b_0$ ,  $b_1$ , and  $b_2$ . This blending of various coupled influences reiterates the need to fit the algebraic model parameters to field data in a real canopy. The above discussion illustrates how the parameterization designed for a single blade can account for canopy effects.

Although this study's numerical model sought to mimic an individual blade, the inputs to the model could be adjusted to better approximate the blade motion and wave attenuation in a canopy. This would be accomplished by inputting fluid velocities that more accurately approximate the flows in a canopy, rather than velocities observed for undisturbed waves. These velocities could be acquired in two different ways: by measuring a phase-averaged velocity profile inside a physical canopy, or by coupling the model with the momentum equation for the fluid and iteratively solving for the blade and fluid motion. Either method would add significant cost beyond what is required for individual blade runs. This cost must be weighed against the benefit of more accurately mimicking the natural system. It is also important to consider the fact that uncertainty in blade parameters may be a significant factor. In this study, the single blade numerical model runs were used to develop the algebraic model and tuning to a canopy is left as part of fitting the model parameters.

*Applying the proposed algebraic model*—The algebraic model parameter values computed in this study are valid only for the specific set of vegetation parameters used in the numerical model runs. In order to apply the algebraic model in the field, site-specific model parameters must first be computed based on field data. An appropriate field experiment would include velocimeters and wave gages separated by a few meters perpendicular to the dominant direction of wave propagation. The velocimeter data would be used to compute  $U_{\text{diff}}$  and  $U_{\text{max}}$ , and the wave gage data would be used to compute wave attenuation. A long time series of these three values in a variety of flow conditions would be used to perform the 2D fit that computes the algebraic model parameters. This approach does not require quadrat sampling or removal of vegetation for rigidity measurements, which would both be required for calculating  $\lambda_R$ .

The model parameters would vary from site to site because they depend on the blade and canopy parameters. Estimating the parameters based on vegetation characteristics is impractical because it would require quadrat sampling and removal of vegetation in order to measure parameters such as canopy spacing and blade rigidity. Using measured velocities and wave attenuation (as suggested in the previous paragraph) is more practical

and more accurate. Because they would be based on direct measurements of wave attenuation, these fits would inherently account for complexities in the coupling between blade and fluid motion. Eventually, many field experiments could be used to develop probability distributions and typical values for the model parameters in different types of vegetation. This type of database, along with mapping of the distribution of vegetation types, would allow the proposed algebraic model to accurately predict wave attenuation in large-scale coastal ocean models.

#### Acknowledgments

We acknowledge W. Sabala for his contribution to the design and assembly of the Environmental Fluid Mechanics Laboratory recirculating wave flume and other laboratory equipment. We also thank two anonymous reviewers and the Associate Editor, C. Stevens, for their exceptionally constructive and helpful comments on earlier versions of this paper.

#### References

- ABDELRHMAN, M. A. 2007. Modeling coupling between eelgrass *Zostera marina* and water flow. *Mar. Ecol. Prog. Ser.* **338**: 81–96, doi:10.3354/meps338081
- BRADLEY, K., AND C. HOUSER. 2009. Relative velocity of seagrass blades: Implications for wave attenuation in low-energy environments. *J. Geophys. Res. Earth Surf.* **114**: F01004, doi:10.1029/2007JF000951
- CHEN, S. N., L. P. SANFORD, E. W. KOCH, F. SHI, AND E. W. NORTH. 2007. A nearshore model to investigate the effects of seagrass bed geometry on wave attenuation and suspended sediment transport. *Estuar. Coast.* **30**: 296–310, doi:10.1007/BF02700172
- DALRYMPLE, R. A., J. T. KIRBY, AND P. A. HUANG. 1984. Wave diffraction due to areas of energy dissipation. *J. Waterway, Port, Coastal, Ocean Eng.* **110**: 67–79, doi:10.1061/(ASCE)0733-950X(1984)110:1(67)
- DEAN, R. G., AND R. A. DALRYMPLE. 1991. *Water wave mechanics for scientists and engineers*. World Scientific.
- DENNY, M. W., B. GAYLORD, B. HELMUTH, AND T. DANIEL. 1998. The menace of momentum: Dynamic forces on flexible organisms. *Limnol. Oceanogr.* **43**: 955–968, doi:10.4319/lo.1998.43.5.0955
- DUARTE, C. M. 2002. The future of seagrass meadows. *Environ. Conserv.* **29**: 192–206, doi:10.1017/S0376892902000127
- FINNIGAN, J. 2000. Turbulence in plant canopies. *Ann. Rev. Fluid Mech.* **32**: 519–571, doi:annurev.fluid.32.1.519
- FONSECA, M. S., AND J. A. CAHALAN. 1992. A preliminary evaluation of wave attenuation by four species of seagrass. *Estuar. Coast. Shelf Sci.* **35**: 565–576, doi:10.1016/S0272-7714(05)80039-3
- , AND J. S. FISHER. 1986. A comparison of canopy friction and sediment movement between 4 species of seagrass with reference to their ecology and restoration. *Mar. Ecol. Prog. Ser.* **29**: 15–22, doi:10.3354/meps029015
- , AND W. J. KENWORTH. 1987. Effects of current on photosynthesis and distribution of seagrasses. *Aquat. Bot.* **27**: 59–78, doi:10.1016/0304-3770(87)90086-6
- GHSALBERTI, M. 2005. Momentum and scalar transport in vegetated shear flows. Ph.D. thesis. Massachusetts Institute of Technology.
- , AND H. M. NEPF. 2002. Mixing layers and coherent structures in vegetated aquatic flows. *J. Geophys. Res. Oceans* **107**: 3011, doi:10.1029/2001JC000871
- INFANTES, E., A. ORFILA, G. SIMARRO, J. TERRADOS, M. LUHAR, AND H. NEPF. 2012. Effect of a seagrass (*Posidonia oceanica*) meadow on wave propagation. *Mar. Ecol. Prog. Ser.* **456**: 63–72, doi:10.3354/meps09754

- KOBAYASHI, N., A. RAICHLE, AND T. ASANO. 1993. Wave attenuation by vegetation. *J. Waterway, Port, Coastal, Ocean Eng.* **119**: 30–48, doi:10.1061/(ASCE)0733-950X(1993)119:1(30)
- LOWE, R., J. KOSEFF, AND S. MONISMITH. 2005. Oscillatory flow through submerged canopies: 1. Velocity structure. *J. Geophys. Res.* **110**: C10016, doi:10.1029/2004JC002788
- LUHAR, M., S. COUTU, E. INFANTES, S. FOX, AND H. NEFF. 2010. Wave-induced velocities inside a model seagrass bed. *J. Geophys. Res. Oceans* **115**: C12005, doi:10.1029/2010JC006345
- , E. INFANTES, A. ORFILA, J. TERRADOS, AND H. M. NEFF. 2013. Field observations of wave-induced streaming through a submerged seagrass (*Posidonia oceanica*) meadow. *J. Geophys. Res. Oceans* **118**: 1955–1968, doi:10.1002/jgrc.20162
- , AND H. NEFF. 2011. Flow-induced reconfiguration of buoyant and flexible aquatic vegetation. *Limnol. Oceanogr.* **56**: 2003–2017, doi:10.4319/lo.2011.56.6.2003
- MENDEZ, F., AND I. LOSADA. 2004. An empirical model to estimate the propagation of random breaking and nonbreaking waves over vegetation fields. *Coast. Eng.* **51**: 103–118, doi:10.1016/j.coastaleng.2003.11.003
- MULLARNEY, J. C., AND S. M. HENDERSON. 2010. Wave-forced motion of submerged single-stem vegetation. *J. Geophys. Res.* **115**: C12061, doi:10.1029/2010JC006448
- NEFF, H. M. 2012. Flow and transport in regions with aquatic vegetation. *Annu. Rev. Fluid Mech.* **44**: 123–142, doi:10.1146/annurev-fluid-120710-101048
- OUDE, R. 2010. Modelling wave attenuation by vegetation with SWAN-VEG: Model evaluation and application to the Noordwaard polder. M.S. thesis. Univ. Twente.
- PETERSON, C. H., R. A. LUETTICH, JR., F. MICHELI, AND G. A. SKILLETER. 2004. Attenuation of water flow inside seagrass canopies of differing structure. *Mar. Ecol. Prog. Series* **268**: 81–92, doi:10.3354/meps268081
- RIFFE, K. C., S. M. HENDERSON, AND J. C. MULLARNEY. 2011. Wave dissipation by flexible vegetation. *Geophys. Res. Lett.* **38**: L18607, doi:10.1029/2011GL048773
- SÁNCHEZ-GONZÁLEZ, J. F., V. SÁNCHEZ-ROJAS, AND C. D. MEMOS. 2011. Wave attenuation due to *Posidonia oceanica* meadows. *J. Hydrol. Res.* **49**: 503–514, doi:10.1080/00221686.2011.552464
- SHORT, F., T. CARRUTHERS, W. DENNISON, AND M. WAYCOTT. 2007. Global seagrass distribution and diversity: A bioregional model. *J. Exp. Mar. Biol. Ecol.* **350**: 3–20, doi:10.1016/j.jembe.2007.06.012
- UTTER, B., AND M. DENNY. 1996. Wave-induced forces on the giant kelp *Macrocystis pyrifera* (Agardh): Field test of a computational model. *J. Exp. Biol.* **199**: 2645–2654.
- WARD, L. G., W. M. KEMP, AND W. R. BOYNTON. 1984. The influence of waves and seagrass communities on suspended particulates in an estuarine embayment. *Mar. Geol.* **59**: 85–103, doi:10.1016/0025-3227(84)90089-6
- WEITZMAN, J. S. 2013. Current- and wave-driven flow and nutrient exchange in natural and model submerged vegetated canopies. Ph.D. thesis. Stanford Univ.
- , K. AVENI-DEFORGE, J. R. KOSEFF, AND F. I. M. THOMAS. 2013. Uptake of dissolved inorganic nitrogen by shallow seagrass communities exposed to wave-driven unsteady flow. *Mar. Ecol. Prog. Ser.* **475**: 65–83, 2013, doi:10.3354/meps09965

Associate editor: Craig L. Stevens

Received: 18 April 2013  
 Accepted: 14 October 2013  
 Amended: 16 October 2013